EUROPEAN ORGANISATION FOR NUCLEAR RESEARCH (CERN)

Search for pair-production of vector-like quarks in pp collision events at $\sqrt{s} = 13$ TeV with at least one leptonically decaying Z boson and a third-generation quark with the ATLAS detector

The ATLAS Collaboration

A search for the pair-production of vector-like quarks optimized for decays into a Z boson and a third-generation Standard Model quark is presented, using the full Run 2 dataset corresponding to 139 fb^{-1} of pp collisions at $\sqrt{s} = 13$ TeV, collected in 2015–2018 with the ATLAS detector at the Large Hadron Collider. The targeted final state is characterized by the presence of a Z boson with high transverse momentum, reconstructed from a pair of same-flavour leptons with opposite-sign charges, as well as by the presence of b-tagged jets and high-transverse-momentum large-radius jets reconstructed from calibrated smaller-radius jets. Events with exactly two or at least three leptons are used, which are further categorized by the presence of boosted W, Z, and Higgs bosons and top quarks. The categorization is performed using a neural-network-based boosted object tagger to enhance the sensitivity to signal relative to the background. No significant excess above the background expectation is observed and exclusion limits at 95% confidence level are set on the masses of the vector-like partners T and B of the top and bottom quarks, respectively. In the singlet model, the limits allow $m_T > 1.27$ TeV and $m_B > 1.20$ TeV. In the doublet model, allowed masses are $m_T > 1.46$ TeV and $m_B > 1.32$ TeV. In the case of 100% branching ratio for $T \rightarrow Zt$ and 100% branching ratio for $B \rightarrow Zb$, the limits allow $m_T > 1.60$ TeV and $m_B > 1.42$ TeV, respectively.

Contents

1 Introduction

The Standard Model (SM) has had astonishing success in describing the interactions of elementary particles, culminating in the discovery [1, 2] of the Higgs boson by the ATLAS and CMS collaborations. Nevertheless, there remain some shortcomings, such as the quadratically divergent corrections predicted to contribute to the square of the Higgs boson mass [3]. In many theories beyond the SM, including Composite Higgs [4, 5] and Little Higgs [6, 7] models, a recurrent theme that addresses these issues is the existence of vector-like quarks (VLQs): coloured spin-1/2 fermions that have left- and right-handed components transforming identically under the SM gauge group. In such models, VLQs are often assumed to couple preferentially to a third-generation quark [8–11], potentially regulating the divergent corrections. The VLQs therefore decay into SM quarks and a W/Z (V) or Higgs (H) boson, with branching ratios (BR) that depend on the VLQ masses and their configuration in weak-isospin multiplets. In renormalizable extensions of the SM that include VLQs, the canonical representation of VLQs constitutes one of seven multiplets: two singlets, three doublets, and two triplets. Vector-like partners, T and B, of the top and bottom quarks can exist with electric charges $(2/3)e$ and $-(1/3)e$, respectively, and can be arranged in singlets, doublets, and triplets. VLQs with exotic charges can also exist, namely X and Y with electric charges $(5/3)e$ and $-(4/3)e$, respectively, which can be arranged in doublets and triplets with the T and B. Assuming an almost degenerate VLQ mass hierarchy [11], the singlet and triplet representations are phenomenologically similar in terms of chiral structure and BR composition. As a consequence, the singlet and doublet representations are those that are primarily assumed in searches at the Large Hadron Collider (LHC). While models with extreme values of 100% BR for decay into a third-generation quark and either a W/Z boson or a Higgs boson are often used as benchmarks, intermediate BR configurations are expected in the more physically motivated singlet and doublet models. In the former, the BR for $T \to Zt$ or $B \to Zb$ reaches $\approx$25% at high VLQ masses [11]. For the (T, B) and (X, T) doublets the BR for $T \to Zt$ reaches $\approx$50% [11], as does the BR for $B \to Zb$ for the (B, Y) doublet.

VLQs were searched for at ATLAS and CMS focusing mainly on the pair-production mode [12–24]. Constraints on VLQ production were also derived recently [25] from a range of differential cross-section measurements at the LHC, complementing the direct searches. VLQ pair production, proceeding primarily
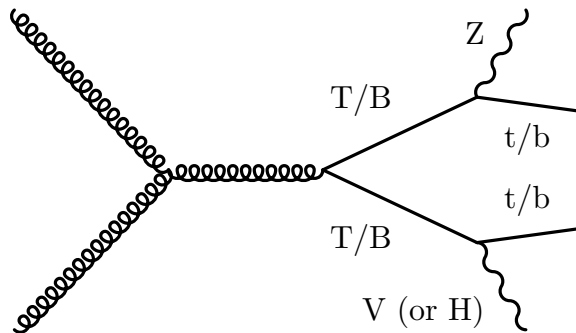
Figure 1: Feynman diagram showing the pair production of *T* or *B* quarks in which at least one of the VLQs decays into a *Z* boson in association with a SM *t*- or *b*-quark, respectively. In this analysis, events in which the *Z* boson decays into a pair of electrons or a pair of muons are targeted. At least one *b*-tagged jet is required to be present after pair production of either type of VLQ, and additional leptons can be produced in the decays of *V* (*W*/*Z*), or *H* bosons on the second leg of the VLQ pair production.

via the strong interaction with a cross-section that depends only on the VLQ mass, is expected to be the dominant mode for masses up to approximately 1 TeV. The most stringent limits at 95% confidence level (CL) on *T* and *B* masses depend on the assumed BR configuration; for 100% BR for $T \rightarrow Zt$, $T \rightarrow Ht$, $T \rightarrow Wb$, and $B \rightarrow Wt$, masses up to 1.36 TeV, 1.43 TeV, 1.35 TeV, and 1.35 TeV are excluded, respectively [12]. For 100% BR for $B \rightarrow Zb$ and $B \rightarrow Hb$, *B* masses up to 1.39 TeV and 1.57 TeV are excluded, respectively [20]. A singlet *T* is excluded for masses below 1.31 TeV and a singlet *B* is excluded for masses below 1.22 TeV, while in the (*T*, *B*) doublet case, *T* and *B* masses below 1.30 TeV are excluded [12, 25]. Single VLQ production has also been searched for [13, 15, 26–30], but the interpretation [31] of the search results depends on an additional coupling constant for the coupling to electroweak bosons.

This Letter presents a search for pair production of *T* and *B* in events with at least two electrons or muons where at least two same-flavour leptons with opposite-sign charges originate from the decay of a *Z* boson. Various BR configurations for the decay of the VLQ into a *V* or *H* boson and a third-generation quark are considered, including the singlet and doublet models, and it is assumed that the VLQ signal kinematics are similar for different configurations. It is further assumed that the production of VLQ pairs is dominated by the strong interaction and that the contribution from electroweak processes is negligible. A diagram illustrating the targeted event topologies is shown in Figure 1. The search is performed across several different event categories included in a maximum-likelihood fit, improving on a previous ATLAS search [13] in the same final state. In addition to benefiting from the larger dataset, the search is also improved by the use of a deep neural network (DNN) to classify the jets in each event as originating from either a *Z* or *W* boson, *H* boson, or top quark.

2 ATLAS detector

ATLAS [32] is a multipurpose particle detector at the Large Hadron Collider (LHC) with a forward–backward symmetric cylindrical geometry and a near 4π coverage in solid angle.[1] It consists of an

---

[1] ATLAS uses a right-handed coordinate system with its origin at the nominal interaction point (IP) in the centre of the detector and the *z*-axis along the beam pipe. The *x*-axis points from the IP to the centre of the LHC ring, and the *y*-axis points

inner tracking detector (ID) [33, 34] surrounded by a thin superconducting solenoid providing a 2 T axial magnetic field, electromagnetic and hadron calorimeters, and a muon spectrometer (MS). The ID covers the pseudorapidity range $|\eta| < 2.5$ and consists of silicon pixel, silicon microstrip, and transition radiation tracking detectors. Lead/liquid-argon (LAr) sampling calorimeters provide electromagnetic (EM) energy measurements with high granularity. A steel/scintillator-tile hadronic calorimeter covers the central pseudorapidity range ($|\eta| < 1.7$). The endcap and forward regions are instrumented with LAr calorimeters for both EM and hadronic energy measurements up to $|\eta| = 4.9$. The MS surrounds the calorimeters and uses three large air-core toroidal superconducting magnets with eight coils each. The field integral of the toroids ranges between 2.0 and 6.0 T m across most of the detector. The MS includes a system of precision chambers for tracking and fast detectors for triggering [35]. A two-level trigger system is used to select events. The first-level trigger is implemented in hardware and uses a subset of the detector information to accept events at a rate below 100 kHz. This is followed by a software-based trigger that reduces the accepted event rate to 1 kHz on average depending on the data-taking conditions. An extensive software suite [36] is used in the reconstruction and analysis of real and simulated data, in detector operations, and in the trigger and data acquisition systems of the experiment.

3 Data and simulated event samples

The analysed dataset comprises pp collisions at a centre-of-mass energy $\sqrt{s} = 13$ TeV recorded by ATLAS between 2015 and 2018 with all detector subsystems operational and with the LHC operating in stable beam conditions with 25 ns bunch spacing. The combined Run 2 dataset corresponds to an integrated luminosity of 139 fb^{-1} with an average of about 34 simultaneous interactions per bunch crossing (pile-up).

All the nominal Monte Carlo (MC) simulation samples used in the analysis were produced with the ATLAS full-simulation framework [37] based on Geant4 [38]. In all samples, pile-up was modelled by combining simulated inelastic pp events with the physics event. The nominal sample for Z boson production in association with jets (Z+jets) was generated with Sherpa 2.2.1 [39–42] and the nominal diboson (VV) sample was generated with Sherpa 2.2.2, with the NNPDF3.0 [43] next-to-next-to-leading-order (NNLO) parton distribution function (PDF) set. The Z+jets sample includes events generated with up to two partons at next-to-leading order (NLO) and up to four partons at leading order (LO) and is normalized to the NNLO cross-section [44]. The VV sample is normalized to the Sherpa NLO cross-section and includes $q\bar{q}$-initiated events with up to one parton at NLO and up to three partons at LO and gg-initiated processes generated using LO matrix elements for up to one additional jet. For both samples, Comix [41] and OpenLoops [45] were used and the matrix element (ME) was merged with the Sherpa parton shower [42] according to the MEPS@NLO prescription [46]. To estimate modelling uncertainties for these backgrounds, additional samples were produced with MadGraph5_aMC@NLO 2.2.3 [47], using the NNPDF3.0nlo PDF set and interfaced to Pythia 8.210 [48] with the A14 set of tuned parameters (tune) [49] and the NNPDF2.3lo PDF for showering.

The nominal SM $t\bar{t}$ background sample uses the Powheg method [50, 51] implemented in Powheg Box v2 [52, 53] with the NNPDF3.0nnlo PDF set. Powheg Box was interfaced with Pythia 8.230 with the A14 tune for showering. The sample is normalized to the NNLO cross-section in QCD including resummation of next-to-next-to-leading logarithmic (NNLL) soft gluon terms calculated with Top++ [54–60]. For the

---

upwards. Cylindrical coordinates (r, ϕ) are used in the transverse plane, ϕ being the azimuthal angle around the z-axis. The pseudorapidity is defined in terms of the polar angle θ as $\eta = -\ln\tan(\theta/2)$. Angular distance is measured in units of $\Delta R \equiv \sqrt{(\Delta\eta)^2 + (\Delta\phi)^2}$.

evaluation of modelling uncertainties, samples were produced with the same ME generator as the nominal sample, but Herwig 7 was used with the H7-UE-MMHT tune [61] for the showering. Additional samples were generated with MadGraph5_aMC@NLO 2.3.3 and the NNPDF3.0nnlo PDF set, using the same showering configuration as the nominal sample.

The nominal sample including $t\bar{t}$ production in association with a vector boson ($t\bar{t} + X$) was generated with MadGraph5_aMC@NLO 2.3.3 interfaced with Pythia 8.210 for showering, using the NNPDF2.3lo PDF set and the A14 tune. The sample includes $t\bar{t} + Z$ and $t\bar{t} + W$ events normalized to the NLO cross-sections calculated with MadGraph5_aMC@NLO. To evaluate modelling uncertainties, samples were produced using Sherpa 2.2.1. Alternative samples were also produced with the nominal sample's ME generator, and in these samples either the A14 tune was varied or Herwig 7 was used with the H7-UE-MMHT tune for the showering. The nominal $t\bar{t} + X$ sample also includes $t\bar{t}t\bar{t}$ and $t\bar{t}WW$ events generated at LO and normalized to cross-sections calculated [47, 62] with NLO QCD and EW corrections.

The single-top processes were simulated with Powheg Box [63, 64] using the NNPDF3.0nlo PDF set and interfaced to Pythia 8.234 with the A14 tune. The samples are normalized to their respective NLO QCD cross-sections [65, 66] for the t-channel and s-channel, and with additional NNLL soft gluon terms for Wt production [67–69]. The diagram-removal scheme [70] was used in the generation of Wt events to address overlaps with the $t\bar{t}$ sample.

Signal samples for the pair production of T and B quarks were generated with Protos [71] interfaced with Pythia 8.186 using the NNPDF2.3lo PDF set and the A14 tune. Masses from 600 GeV to 2 TeV were simulated in the singlet model, but with the BR for each of the three decays to a vector or Higgs boson fixed to 1/3 for all samples. A BR reweighting procedure is performed event-by-event in order to achieve any BR configuration for a given VLQ mass, including the configurations expected for the doublet models. Dedicated signal samples in the doublet models for the 700 GeV and 1.2 TeV mass points were also produced to validate the reweighting procedure and to verify that the singlet and doublet signal kinematics are indistinguishable in the analysis as is assumed. The signal sample cross-sections were calculated with Top++ at NNLO+NNLL in QCD using the MSTW2008nnlo [72–74] PDF set.

4 Object reconstruction

Events are required to have at least one vertex candidate with at least two tracks with transverse momentum $p_T > 0.5$ GeV. The primary vertex (PV) is defined to be the candidate with the largest Σp_T^2, where the sum is performed over all associated tracks.

Electrons are reconstructed [75] from clusters in the EM calorimeter matched with ID tracks and must fulfil the *tight likelihood* identification criteria [75]. Electrons are calibrated [75] and are required to have $p_T > 28$ GeV and to be reconstructed within $|\eta| < 2.47$, excluding the barrel–endcap transition regions ($1.37 < |\eta| < 1.52$). In order to maintain a high acceptance for the expected signal events, no isolation requirements are applied to electron candidates beyond those implicit in the trigger requirements. Furthermore, electron candidates must be associated with the PV by requiring that the longitudinal impact parameter with respect to the PV satisfies $|z_0 \cdot \sin\theta| < 0.5$ mm and that the transverse impact parameter with respect to the beamline (d_0) has a significance $|d_0|/\sigma(d_0) < 5$.

Muons are reconstructed [76] from combined tracks in the MS and the ID and must fulfil *medium* identification criteria [76]. Muons are calibrated and are required to have $p_T > 28$ GeV and to be reconstructed within $|\eta| < 2.5$. Muon candidates must also satisfy the track-based isolation requirements

defined by the *FixedCutTightTrackOnly* working point [76]. This working point uses the scalar sum of the p_T of all tracks that are within a cone of size $\Delta R = \min\{0.3, 10\,\text{GeV}/p_T(\mu)\}$ around the muon candidate, where $p_T(\mu)$ is the candidate muon p_T. The track associated with the muon candidate under consideration is excluded from the sum. The muon is selected if this sum is less than 15% of $p_T(\mu)$. Finally, muon candidates are required to have $|z_0 \cdot \sin\theta| < 0.5\,\text{mm}$ and a d_0 significance smaller than 3.

Jets are reconstructed using the anti-k_t algorithm [77, 78] with a radius parameter of 0.4 from topological clusters of energy deposits in the calorimeter [79, 80]. Jets are calibrated to an energy scale obtained from a combination of simulation-based corrections and measurements in data [81] and are required to fulfil $p_T > 25\,\text{GeV}$ for $|\eta| < 2.5$ and $p_T > 35\,\text{GeV}$ for $2.5 < |\eta| < 4.5$. To reduce jet contributions from pile-up, a 'jet vertex tagger' algorithm using a two-dimensional likelihood discriminant [82] is applied to jets with $|\eta| < 2.4$ and $p_T < 60\,\text{GeV}$. The MV2c10 algorithm [83] is used to identify jets in the central region ($|\eta| < 2.5$) containing a b-hadron decay (b-tagging) with a working point corresponding to a b-tagging efficiency in simulated $t\bar{t}$ events of 77%, a c-jet rejection factor of ~6, and a light-jet rejection factor of ~130.

The missing transverse momentum [84], with magnitude E_T^{miss}, is defined as the negative vectorial sum of the transverse momenta of all the calibrated reconstructed lepton and jet candidates in the event and includes a 'soft term' with contributions from tracks emanating from the PV but not associated with any of the reconstructed objects.

A procedure to remove potential overlaps between reconstructed leptons and jets is performed sequentially as follows. First, any muon that leaves energy deposits in the calorimeters and shares a track in the ID with an electron is removed. After such muons have been removed, any electron sharing an ID track with one of the remaining muons is removed. Next, any jet within $\Delta R = 0.2$ of an electron is removed, followed by the removal of electrons within $\Delta R = 0.4$ of any remaining jet. Subsequently, any jet with at most two tracks with $p_T > 0.5\,\text{GeV}$ within $\Delta R = 0.2$ of a muon is removed, unless it has been b-tagged. At the end of the procedure, any muon within $\Delta R = \min\{0.4, 0.04 + 10\,\text{GeV}/p_T(\mu)\}$ of any remaining jet is removed.

Finally, large-radius 'reclustered' (RC) jets [85] are reconstructed by applying the anti-k_t algorithm with a radius parameter of 1.0, using the set of selected and already calibrated smaller-radius jets defined above. To reduce dependence on pile-up, the RC jets are trimmed [86] by removing all constituent jets with p_T below 5% of the RC jet p_T. These RC jets are used only for event categorization, and therefore no additional checks for potential overlaps with the previously defined objects are performed.

5 Event selection and categorization

An initial preselection of events is performed as follows. Events are required to satisfy at least one of the single-lepton triggers operating during Run 2 [35, 87, 88]. These triggers had varying p_T thresholds for electrons and muons for different data-taking periods, as well as isolation requirements that were typically more relaxed with increasing p_T threshold. Events are additionally required to have at least two opposite-sign-charge, same-flavour (OS-SF) leptons and to have at least two jets in the central region. The pair of OS-SF leptons with an invariant mass $m(\ell\ell)$ closest to $m_Z = 91.2\,\text{GeV}$ is referred to as 'the Z boson candidate' and only events with $|m(\ell\ell) - m_Z| < 10\,\text{GeV}$ are kept.
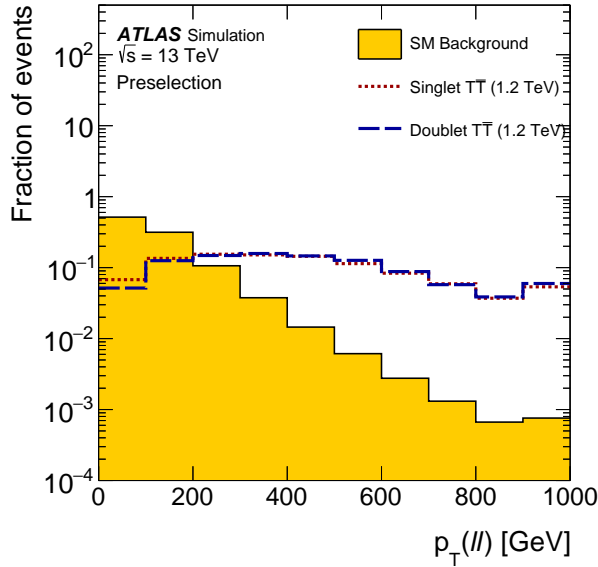
Preselected events are divided into two orthogonal and individually optimized channels: one requiring exactly two leptons (dilepton, labelled as '2ℓ') and a second requiring at least three leptons (trilepton, labelled as '3ℓ'). The channels are combined statistically to obtain the final result, taking advantage of the
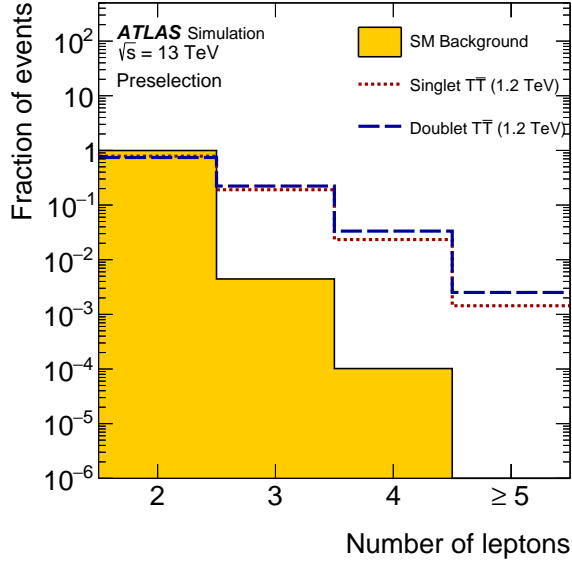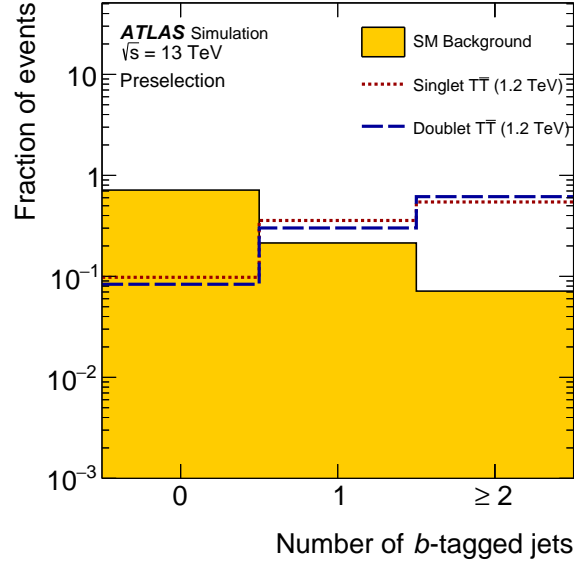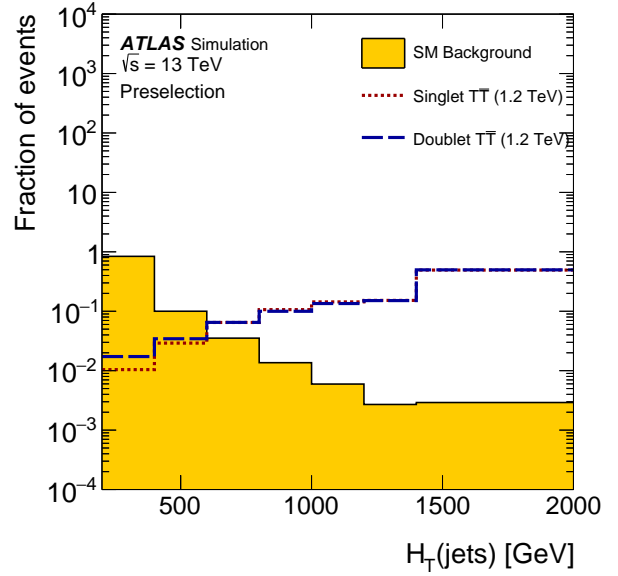
Figure 2: Distributions, normalized to unit area, obtained from MC simulation for the sum of all the background processes (solid area) and for benchmark signal processes (dashed lines): (a) lepton multiplicity, (b) b-tagged jet multiplicity, (c) transverse momentum of the Z boson candidate, $p_\mathrm{T}(\ell\ell)$, and (d) scalar sum of the jet transverse momenta, $H_\mathrm{T}(\mathrm{jet})$. The signal processes concern the pair production of vector-like T or B quarks with a mass of 1.2 TeV. The last bin contains the overflow.
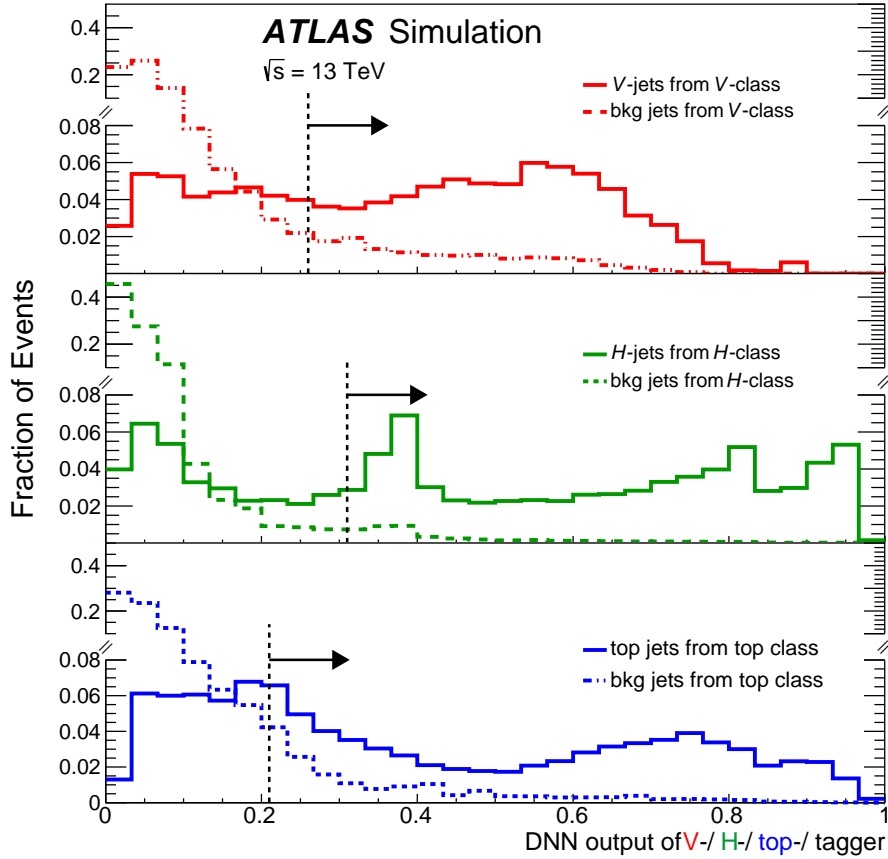
Figure 3: The distributions of the DNN output of MCBOT for the V boson, H boson, and top quark classes for RC jets with p_T between $150\,\text{GeV}$ and $1\,\text{TeV}$. For each tagger (V, H, or top) the response to the corresponding signal jets (solid lines) is compared with the response to the background jets (dashed lines). The responses to signal jets other than the corresponding signal for each tagger are not shown for simplicity. Signal jets are defined by geometrically matching the RC jets to the corresponding generator-level particles. Background jets are obtained from multijet events. The colours red, green, and blue indicate the DNN output values for the V-, H-, or top-tagger, respectively. The RC jet p_T is reweighted together with the RC jet η to be uniform over the full range. All distributions are normalized to unit area. The y-axis is split for better readability.

relatively high signal acceptance achieved by the 2ℓ channel and the higher signal purity offered by the 3ℓ channel.

Figure 2 shows distributions of example kinematic variables for the expected background and for benchmark signal processes obtained from MC simulation. In addition to the lepton multiplicity, the analysis exploits the high multiplicities of jets, large-radius jets, and b-tagged jets expected for pair-produced VLQ signal. Requirements on the momentum of the Z boson candidate, $p_T(\ell\ell)$, and the scalar sums of the transverse momenta of objects reconstructed in the events, H_T, are applied to suppress the background. Furthermore, the analysis uses RC jets as an input to a 'multi-class boosted object tagger' (MCBOT) in order to identify (tag) the origin of each RC jet as being either a hadronically decaying V boson, H boson, or top quark.

MCBOT is based on a multi-class DNN using the Keras [89] and TensorFlow [90] software libraries. The DNN is trained using RC jets from simulated $Z' \rightarrow t\bar{t}$ events, $W' \rightarrow WZ$ events, and events with a Kaluza–Klein graviton in the bulk Randall–Sundrum model [91] decaying into a pair of H bosons which

each decay into $b\bar{b}$ with a BR fixed to 100%. These dedicated events are generated so that RC jets with a mass of at least 40 GeV are uniformly distributed in an RC jet p_T range between 150 GeV and 3 TeV. The three signal labels (V, H, top) are assigned by matching the RC jet to the corresponding hadronically decaying boson or top quark within a ΔR of 0.75 at generator level. Simulated multijet events are used to obtain the RC jets with a *background* label. The RC jets in these four classes are reweighted such that their distributions are uniform in RC jet p_T and η. The 18 input variables of the DNN are the RC jet p_T and mass, the number of the RC jet constituent smaller-radius jets, the four-momentum vectors of the three highest-p_T constituent jets, and the b-tagging decisions for those three jets. The DNN consists of four fully connected hidden layers with Rectified Linear Unit [92] activation functions and a four-dimensional output layer in which nodes are activated using the *softmax* [93] function. The first hidden layer uses 32 nodes, reduced to 27, 14, and 12 nodes for the second, third, and fourth hidden layer, respectively. The ADAM [94] optimizer is used to minimize the categorical cross-entropy as a loss function in order to find the optimal weights. The set of hyper-parameters as optimized for a related ATLAS analysis [14] is used. The projections of the four-dimensional output of the DNN are used to define a working point for each of the signals in order to define a V-tag, a H-tag, and a top-tag. Figure 3 shows an example set of these projections for RC jets with p_T between 150 GeV and 1 TeV. In cases where the same RC jet satisfies the requirements for more than one tag, the tag with the highest neural-network output value is retained. Therefore, at most one signal label can be assigned to any RC jet. For the selected working point, and for $T\bar{T}$ signal with $m_T = 1400$ GeV in the singlet configuration, efficiencies of 55%, 41%, and 54% are measured for V, H, and top signals, respectively.

In the 2ℓ channel, events are required to satisfy $p_T(\ell\ell) > 300$ GeV in order to select leptonic Z boson candidates originating from the decay of a heavy VLQ. In addition, given the large amount of jet activity expected in signal events and to take advantage of a potentially invisible decay of the Z boson in the decay chain of the second VLQ in the pair, requirements are placed on the scalar sum of the jet transverse momenta, $H_T(\text{jet})$, and E_T^{miss}. Two exclusive signal regions (SR) are defined by requiring $H_T(\text{jet}) + E_T^{\text{miss}} > 1380$ GeV and either exactly one b-tagged jet (1b SR) or at least two b-tagged jets (2b SR). The chosen kinematic requirements are motivated by the selection criteria of the earlier ATLAS analysis [13] and are optimized using a procedure that maximizes the expected sensitivity for a few benchmark signal models. The most relevant event selection criteria are shown in Table 1, which additionally shows the definitions of the signal regions and background control regions. The events in each SR are divided into exclusive categories based on combinations of the numbers of signal-tagged RC jets of various types identified by MCBOT. A signal significance optimization procedure is used to group the possible tagging combinations so as to reduce the set of categories to seven, as shown in Table 2. These include 'Double tag' categories with different combinations of at least two RC jets with tags of any signal type, as well as a final 'Overflow' category that includes events with more than two tags but also leftover two-tag combinations that are not included in the former categories. In order to recover some of the events in which RC jets might be misidentified, combinations with more than one V or H boson are included even though one of the two VLQs is required to decay to a leptonically decaying Z boson in the targeted event topology.

In the 3ℓ channel, the Z candidate transverse momentum requirement is relaxed to $p_T(\ell\ell) > 200$ GeV to increase signal efficiency given the significant background suppression due to the three-lepton requirement. To take advantage of the additional lepton activity, events must also satisfy $H_T(\text{jet} + \text{lep}) > 300$ GeV, where $H_T(\text{jet} + \text{lep})$ is the scalar sum of the jet and lepton transverse momenta. Events in the 3ℓ SR are also required to have at least one b-tagged jet and are divided into five exclusive categories based on the number of MCBOT tags, similarly to the 2ℓ channel, as shown in Table 2.

The signal efficiency, defined as the ratio of the number of events selected by the signal regions to the

Table 1: Definitions of analysis regions and the most relevant event selection criteria. The final discriminating variables used in the fit are also indicated for each region: $m(Zb_1)$ and $m(Zb_2)$ refer to the mass of the system of the Z boson candidate and either the leading b-jet or subleading b-jet, respectively. $H_T(\text{jet})$ is defined as the scalar sum of the transverse momenta of all selected jets, while $H_T(\text{jet} + \text{lep})$ is defined as the scalar sum of the transverse momenta of all selected jets and leptons.

Preselection						
	≥ 2 central jets at least two SF leptons with $p_T > 28\,\text{GeV}$ at least one pair of OS-SF leptons $\|m(\ell\ell) - m_Z\| < 10\,\text{GeV}$					
Channel definitions	2ℓ $= 2\ell$ $p_T(\ell\ell) > 300\,\text{GeV}$ $H_T(\text{jet}) + E_T^{\text{miss}} > 920\,\text{GeV}$				3ℓ $\geq 3\ell$ $p_T(\ell\ell) > 200\,\text{GeV}$ $H_T(\text{jet} + \text{lep}) > 300\,\text{GeV}$	
Region definitions	1b SR $H_T(\text{jet}) + E_T^{\text{miss}} > 1380\,\text{GeV}$ $= 1\ b$-jet	2b SR $\geq 2\ b$-jet	1b CR $H_T(\text{jet}) + E_T^{\text{miss}} < 1380\,\text{GeV}$ $= 1\ b$-jet	2b CR $\geq 2\ b$-jet	SR – $\geq 1\ b$-jet	VV CR – $= 0\ b$-jet
MCBOT categories Fitted variable	7 $m(Zb_1)$	7 $m(Zb_2)$	– $H_T(\text{jet}) + E_T^{\text{miss}}$	–	5 $H_T(\text{jet} + \text{lep})$	–

number of events generated in the signal samples, for the benchmark of a 1.2 TeV singlet T, is 0.3% and 0.5% in the 1b and 2b 2ℓ signal regions, respectively, and 0.5% in the 3ℓ signal regions.

The SM background contribution is estimated using MC simulation and is adjusted in the final simultaneous maximum-likelihood fit to the data with the help of signal-depleted control regions (CR), designed to be similar in phase-space to the SR. Leading backgrounds include Z+jets, which is the dominant background for 2ℓ, as well as VV and $t\bar{t} + X$, which are dominant for 3ℓ. Smaller backgrounds include those from $t\bar{t}$, single top quark and four top quark.

The inputs to the fit are binned distributions of final discriminants optimized for each of the two channels. In the 2ℓ channel, in all the 1b SR categories, the invariant mass of the leptonically decaying Z candidate and the leading b-tagged jet, $m(Zb_1)$, is used as a final discriminant, while for the 2b SR categories the subleading b-tagged jet is used instead and the discriminating variable is $m(Zb_2)$. Two 2ℓ CR corresponding to each SR are defined by requiring $920\,\text{GeV} < H_T(\text{jet}) + E_T^{\text{miss}} < 1380\,\text{GeV}$. These CR are not further categorized using MCBOT and participate in the fit using the distribution of $H_T(\text{jet}) + E_T^{\text{miss}}$. In the 3$\ell$ channel a single VV CR is defined by requiring exactly zero b-jets. The final discriminant for all 3ℓ SR categories and for the VV CR is $H_T(\text{jet} + \text{lep})$.

6 Systematic uncertainties

Several experimental and theoretical systematic uncertainties that can affect the normalization or the shape of the fitted distributions are considered. For each considered source of uncertainty, variations representing the -1σ and $+1\sigma$ confidence interval are derived. The analysis selection, including the MCBOT categorization, is applied on each variation to estimate their effect on the final discriminants. Several of these modelling uncertainties are constrained after the fit due to the significantly larger number of events in the control regions compared to the signal regions. However, these constraints do not impact the final limit. Furthermore, the analysis is dominated by statistical uncertainties; the expected lower limits

Table 2: Definitions of the categorization of events in the 2ℓ and 3ℓ channels based on the number of MCBOT tags. Unless otherwise noted, the columns indicate the exact number of required tagged RC jets for each type. Categories labelled as 'Double tag' include combinations with exactly two tags of any type. Categories labelled as 'Overflow (OF)' include all the tagging combinations that are not explicitly included in the other categories.

| Category | 2ℓ channel | | | | | | 3ℓ channel | | |
| | 1b SR | | | 2b SR | | | − | | |
	V-tags	H-tags	top-tags	V-tags	H-tags	top-tags	V-tags	H-tags	top-tags
No tag	0	0	0	0	0	0	0	0	0
V tag	1	0	0	1	0	0	≥ 1	0	0
H tag	0	1	0	0	1	0	0	≥ 1	0
Top tag	0	0	1	0	0	1	0	0	≥ 1
Double tag 1	2	0	0	2	0	0		–	
	0	2	0	0	2	0		–	
	1	0	1	1	1	0		–	
		–		0	0	2		–	
Double tag 2	0	1	1	0	1	1		–	
	0	0	2		–			–	
Overflow (OF)	1	1	0	1	0	1	0	≥ 1	≥ 1
	or > 2 tags			or > 2 tags			≥ 1	0	≥ 1
		–			–		≥ 1	≥ 1	0
		–			–		≥ 1	≥ 1	≥ 1

on the VLQ masses decrease by no more than 4% when all the systematic uncertainties are included in the analysis.

Experimental uncertainties include effects on the electron energy scale and energy resolution [75], the muon momentum scale and resolution [76], as well as uncertainties in the data-to-MC correction factors for the electron and muon trigger, reconstruction, identification, and isolation efficiencies [75, 76]. Jet energy scale and resolution uncertainties are also included, as obtained from studies in data and simulation [81]. A 10% uncertainty [95] is assigned to the small-radius jet mass, which is not calibrated but is used in the RC jet mass calculation. Flavour-tagging uncertainties include uncertainties in the b-jet tagging, c-jet tagging, and light-jet mis-tagging efficiencies, and uncertainties due to extrapolations to regions not covered by the data used for the efficiency measurements [83, 96, 97]. Subdominant uncertainties include uncertainties related to the soft term in the $E_{\mathrm{T}}^{\mathrm{miss}}$ calculation [84] and to the $E_{\mathrm{T}}^{\mathrm{miss}}$ energy scale and resolution, uncertainties in the reweighting of the MC event samples to match the pile-up conditions in data, and a 1.7% [98] uncertainty in the integrated luminosity of the combined 2015–2018 dataset.

Theoretical uncertainties include cross-section and other modelling uncertainties for all background samples. The cross-section uncertainties considered are of order 5% to 6% for the Z+jets, $t\bar{t}$, and VV samples [99, 100] and of order 10% [99] $t\bar{t} + Z$ samples. A conservative 50% uncertainty is used for the $t\bar{t} + W$ sample. Uncertainties due to the choice of generator or showering algorithm are estimated using additional samples from alternative generators. The uncertainties due to the choice of factorization and renormalization scales, the modelling of ISR and FSR, and the choice of PDF set are estimated by varying

the nominal sample via additional generator weights, if available, or by using alternative samples. An additional shape uncertainty is applied to the modelling of the heavy-flavour fraction (HF) of jets in the Z+jets and VV samples. This uncertainty is estimated by separating, using generator-level information, the events with jets originating from b or c quarks from events with jets originating from light quarks and rescaling the HF contribution by 50%. In the 2ℓ channel, the HF uncertainty is uncorrelated between the categories requiring exactly one or at least two b-tagged jets. In the 3ℓ channel, the HF uncertainty is applied in a correlated way across the SR categories and the VV CR, since both regions have the same b-tagging requirements. Uncertainties in the VLQ pair-production cross-section similarly include the independent variation of the factorization and renormalization scales and variations in the PDF and strong coupling constant, following the PDF4LHC [101] prescription with the MSTW 2008 68% CL NNLO, CT10 NNLO [102, 103] and NNPDF2.3 5f FFN PDF sets.

7 Results

The compatibility of the data with the background-only hypothesis or with the signal-plus-background hypothesis is tested with a binned likelihood fit of the discriminating variables in the categories of each individual channel. The uncertainties are included as nuisance parameters (NP) with Gaussian constraints in the likelihood fit. Additional NPs are included to take into account the statistical uncertainties in each bin for each event category due to the limited size of the simulated samples. The likelihood function $L(\mu, \vec{\theta})$ is constructed as a product of Poisson probabilities for each bin in the discriminating variable in each category and depends on the signal-strength factor μ, which multiplies the expected signal cross-section σ, and the set of all NPs $\vec{\theta}$. Test statistics are based on the profile-likelihood ratio $\lambda_\mu = L(\mu, \hat{\hat{\vec{\theta}}}_\mu)/L(\hat{\mu}, \hat{\hat{\vec{\theta}}}_{\hat{\mu}})$ where $\hat{\mu}$ and $\hat{\hat{\vec{\theta}}}_{\hat{\mu}}$ are the values of μ and $\vec{\theta}$ that maximize the likelihood function, and $\hat{\hat{\vec{\theta}}}_\mu$ are the values of $\vec{\theta}$ that maximize the likelihood for a given μ [104]. Hypothesis tests are performed with RooStats [105] with statistical models implemented using RooFit [106] and HistFactory [107]. The fit procedure was first validated in pseudo-data obtained by the sum of the expected background contributions. Subsequently, the procedure and the modelling of the background were tested by including in the fit those categories in which the benchmark signal contribution is expected to be smaller than 3% of the total background. Before the final full unblinding of the data, an additional check was performed by including in the fit all bins in all analysis categories with expected signal contributions smaller than 5% of the total background in those bins.

A background-only fit to the data, in which μ is set to zero, is performed using q_0 [104] as the test statistic and no significant excess over the background expectation is observed. To obtain the final result, a simultaneous fit of all the regions and categories of both channels is performed. The results are found to be insensitive to variations of the correlation model and the following approach was adopted: all experimental and cross-section uncertainties are treated as fully correlated between the two analysis channels, while the remaining, modelling-related, uncertainties are treated as uncorrelated. Figure 4 shows the background and observed data yields in all the analysis categories after the combined background-only fit (post-fit). Post-fit distributions of the fitted variables in the background control regions and in selected signal region categories are shown in Figure 5 for the 2ℓ channel and in Figure 6 for the 3ℓ channel. The figures include the expected distributions for $T\bar{T}$ signal with $m_T = 1.2$ TeV generated in the singlet configuration. The event yields for the dominant backgrounds in each event category after the background-only fit are also summarized in Table 3, which includes the number of events observed in data. The table also includes

the expected yields in number of events for $T\bar{T}$ and $B\bar{B}$ production in the singlet configuration with $m_{\text{VLQ}} = 1.2\,\text{TeV}$. These yields and their uncertainties are provided before any fit is performed (pre-fit).
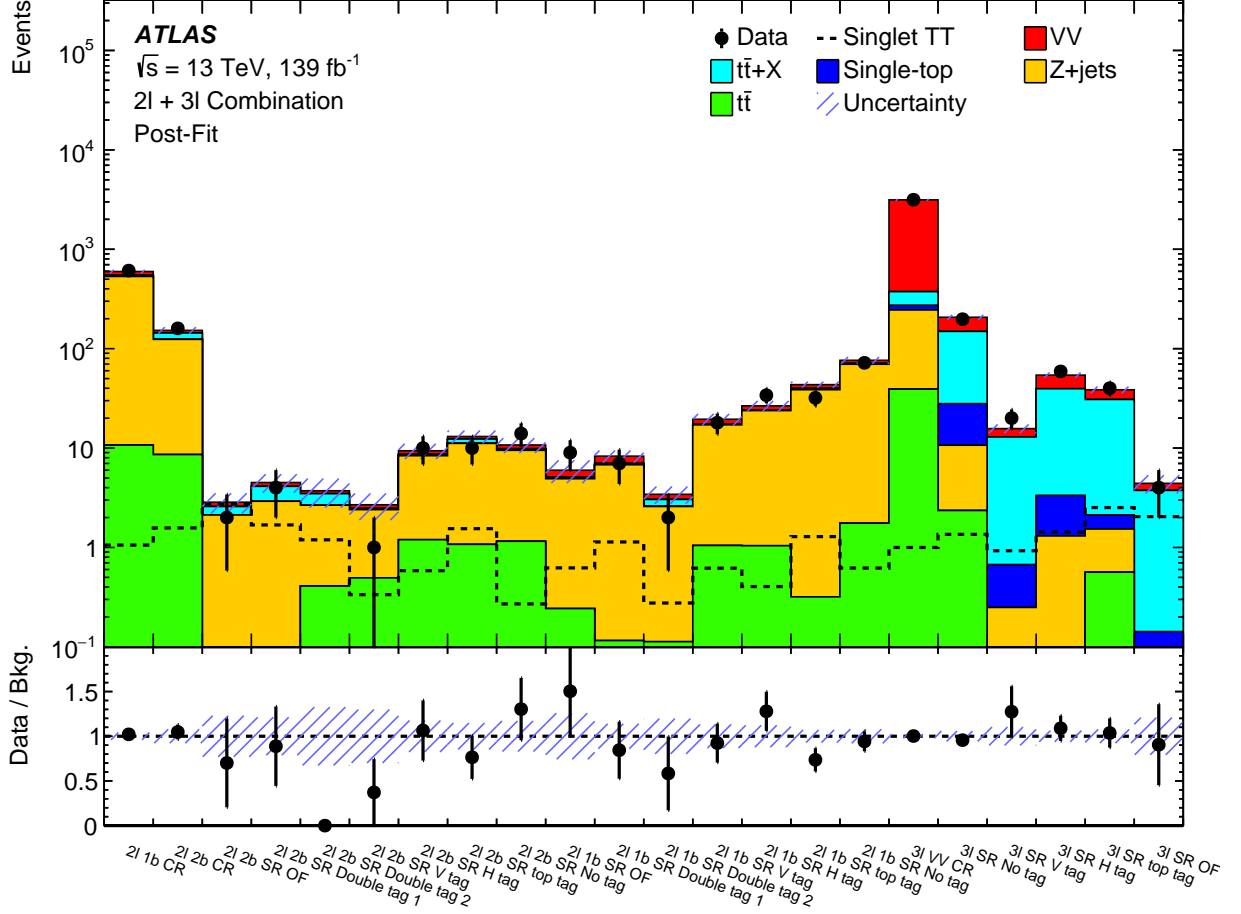

Figure 4: Summary of data and background yields in all analysis categories after the background-only fit. The expected yields for singlet $T\bar{T}$ signal with $m_T = 1.2\,\text{TeV}$ are also shown for comparison. The bottom panel shows the ratio of the data over the total background prediction. The shaded band includes statistical and post-fit systematic uncertainties.

Upper limits on the pair-production cross-section as a function of the VLQ mass are derived at 95% CL for the T and B quarks. These limits are derived by using $\tilde{q}_\mu$ [104] as the test statistic with the CL$_{\text{s}}$ technique [108, 109] in the asymptotic approximation [104]. The limits are found to agree within a few percent with the limits obtained with pseudo-experiments. For the 1σ uncertainty contours, the limits agree within 10%, with the -1σ band being slightly too narrow in the asymptotic approximation and the $+1\sigma$ band being slightly too wide. The expected and observed upper limits on the cross-section obtained from the combination of the two channels are shown in Figure 7. To demonstrate the complementarity of the two channels, their individually obtained expected limits are also shown. Three benchmark scenarios for each of B and T are shown, namely the singlet, doublet, and 100% BR configurations, with increasingly high BR to Zb or Zt. Comparisons with the respective theoretical predictions of the cross-sections give the lowest-allowed VLQ masses as summarized in Table 4. The higher signal purity in the 3ℓ channel results in an overall higher sensitivity for T than in the 2ℓ channel, while the larger data sample and finer categorization of the latter manifests in a performance that is dominant in the results for B. For models
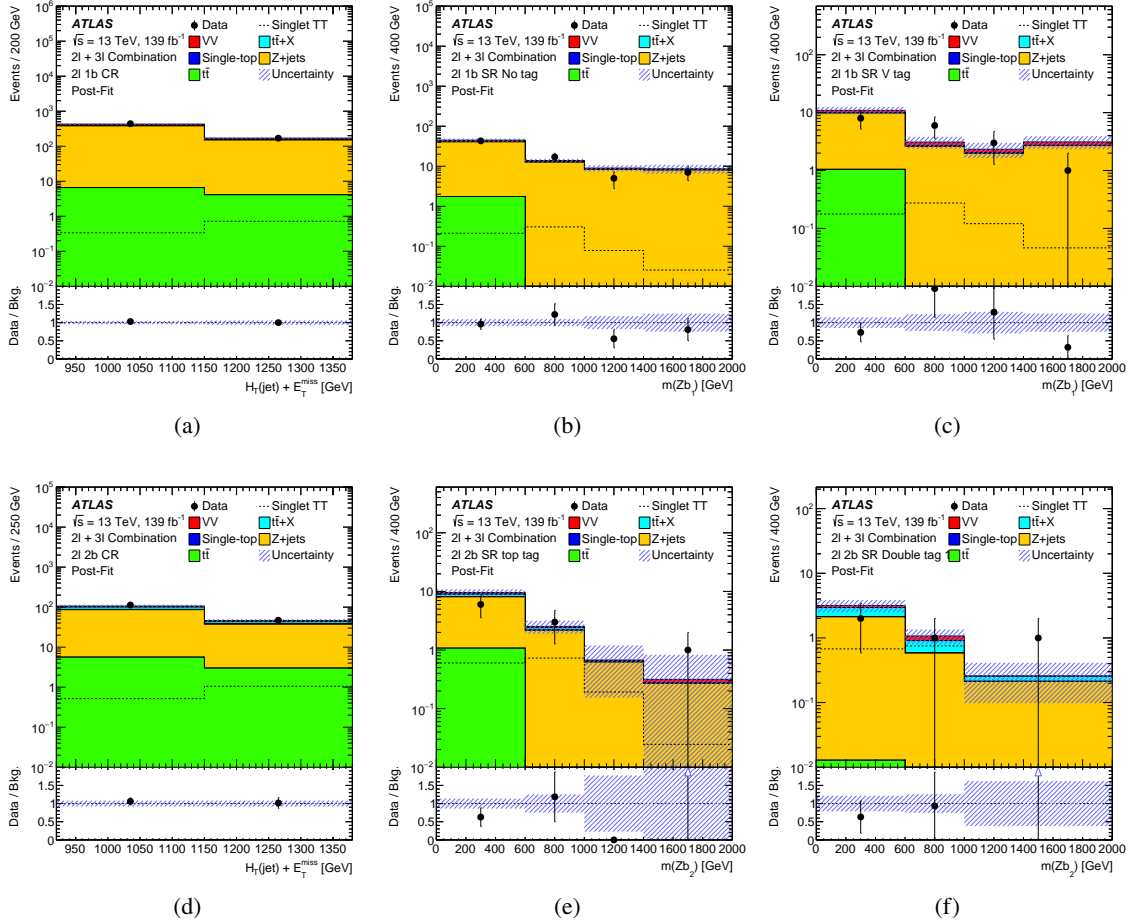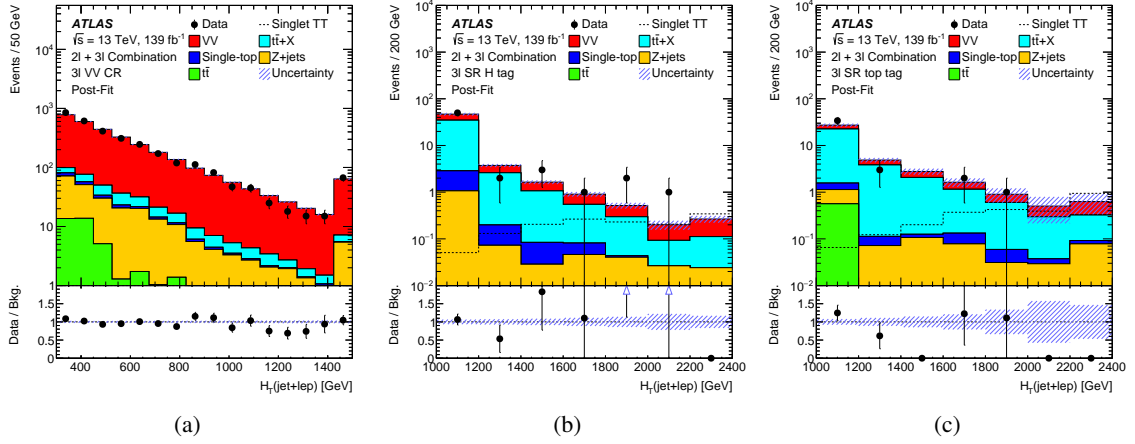
Figure 5: Distributions of the final discriminants for the 2ℓ channel in the control regions and in selected event categories of the signal regions: (a) control region and (b,c) categories requiring exactly one b-jet or (d) control region and (e,f) categories requiring at least two b-jets. The distributions are shown after the combined background-only fit. The distributions expected for singlet $T\bar{T}$ signal with $m_T = 1.2$ TeV are also shown in overlay. The bottom panels show the ratio of the data over the total background prediction. The two blue triangles indicate points beyond the vertical range. The last bin contains the overflow.

Figure 6: Distributions of the final discriminants for the 3ℓ channel in the (a) VV control region and in (b,c) selected event categories of the signal region. The distributions are shown after the combined background-only fit. The distributions expected for singlet $T\bar{T}$ signal with $m_T = 1.2\,\text{TeV}$ are also shown in overlay. The bottom panels show the ratio of the data over the total background prediction. The two blue triangles indicate points beyond the vertical range. The last bin contains the overflow.

Table 3: Summary of observed and predicted yields in the control regions and signal region categories. The background prediction is shown after the combined likelihood fit to data under the background-only hypothesis across all control region and signal region categories. The uncertainties include statistical and systematic uncertainties. Due to correlations, the total background uncertainty is not necessarily equal to the sum in quadrature of the uncertainties of the individual background processes. The expected yields for benchmark signals with $m_{\text{VLQ}} = 1.2\,\text{TeV}$ obtained by using their theoretical cross-sections are also shown with their pre-fit uncertainties. Dashes indicate negligible yields.

Event category	Data	Total background	VV	$t\bar{t} + X$	Single-top	Z+jets	$t\bar{t}$	Singlet $T\bar{T}$ $m_T = 1.2$ TeV	Singlet $B\bar{B}$ $m_B = 1.2$ TeV
2ℓ $1b$ CR	610	598 ± 24	50 ± 18	13 ± 4	1.3 ± 0.6	522 ± 30	11 ± 4	1.06 ± 0.08	1.27 ± 0.09
2ℓ $1b$ SR No tag	72	76 ± 6	5.5 ± 2.0	0.37 ± 0.13	0.8 ± 0.9	68 ± 6	1.8 ± 1.9	0.62 ± 0.13	1.52 ± 0.23
2ℓ $1b$ SR V tag	18	19.6 ± 2.6	2.2 ± 0.8	0.22 ± 0.08	–	16.1 ± 2.1	1.1 ± 1.3	0.63 ± 0.07	1.31 ± 0.13
2ℓ $1b$ SR H tag	34	26.6 ± 3.3	2.4 ± 0.9	0.38 ± 0.09	–	22.8 ± 3.0	1.1 ± 1.5	0.41 ± 0.05	0.66 ± 0.09
2ℓ $1b$ SR top tag	32	43.5 ± 3.1	3.6 ± 1.3	1.25 ± 0.22	–	38.3 ± 3.3	0.3 ± 0.6	1.29 ± 0.14	1.40 ± 0.14
2ℓ $1b$ SR Double tag 1	7	8.3 ± 1.2	1.3 ± 0.5	0.20 ± 0.09	–	6.7 ± 1.0	0.1 ± 0.4	1.14 ± 0.15	1.05 ± 0.17
2ℓ $1b$ SR Double tag 2	2	3.4 ± 0.7	0.39 ± 0.19	0.42 ± 0.10	–	2.5 ± 0.5	0.11 ± 0.31	0.27 ± 0.06	0.19 ± 0.06
2ℓ $1b$ SR OF	9	6.0 ± 1.6	0.9 ± 0.4	0.18 ± 0.05	–	4.7 ± 1.3	0.2 ± 0.7	0.62 ± 0.08	0.60 ± 0.11
2ℓ $2b$ CR	160	152 ± 12	9 ± 4	18 ± 6	1.2 ± 0.6	115 ± 13	9.0 ± 3.5	1.58 ± 0.10	1.90 ± 0.13
2ℓ $2b$ SR No tag	14	10.7 ± 1.9	0.9 ± 0.4	0.07 ± 0.08	0.3 ± 0.5	8.3 ± 1.1	1.2 ± 1.4	0.27 ± 0.07	1.11 ± 0.17
2ℓ $2b$ SR V tag	1	2.7 ± 0.8	0.22 ± 0.13	0.06 ± 0.05	–	1.9 ± 0.5	0.5 ± 0.7	0.34 ± 0.04	0.81 ± 0.08
2ℓ $2b$ SR H tag	10	9.4 ± 1.6	0.76 ± 0.34	0.26 ± 0.09	–	7.1 ± 1.0	1.2 ± 1.4	0.59 ± 0.09	1.90 ± 0.16
2ℓ $2b$ SR top tag	10	13.0 ± 1.9	0.8 ± 0.4	1.10 ± 0.30	–	10.0 ± 1.6	1.1 ± 1.2	1.56 ± 0.18	1.97 ± 0.15
2ℓ $2b$ SR Double tag 1	4	4.5 ± 1.0	0.40 ± 0.25	1.2 ± 0.6	–	2.9 ± 0.8	0.01 ± 0.19	1.71 ± 0.11	1.71 ± 0.18
2ℓ $2b$ SR Double tag 2	0	3.7 ± 1.2	0.25 ± 0.14	0.78 ± 0.18	–	2.3 ± 0.6	0.4 ± 1.1	1.22 ± 0.10	1.12 ± 0.10
2ℓ $2b$ SR OF	2	2.8 ± 0.7	0.28 ± 0.15	0.44 ± 0.20	–	2.1 ± 0.6	–	2.76 ± 0.25	2.02 ± 0.26
3ℓ VV CR	3149	3140 ± 70	2770 ± 90	98 ± 9	26.7 ± 1.6	210 ± 60	40 ± 18	1.00 ± 0.14	0.90 ± 0.14
3ℓ SR No tag	198	203 ± 11	59 ± 5	117 ± 10	17.3 ± 0.6	8.5 ± 3.0	2.4 ± 2.0	1.37 ± 0.17	1.31 ± 0.17
3ℓ SR V tag	20	15.3 ± 1.5	2.82 ± 0.34	11.8 ± 1.5	0.42 ± 0.06	0.25 ± 0.11	–	0.94 ± 0.07	0.71 ± 0.09
3ℓ SR H tag	59	52.9 ± 2.8	14.9 ± 1.2	34.7 ± 2.7	2.03 ± 0.14	1.3 ± 0.4	–	1.44 ± 0.10	0.96 ± 0.08
3ℓ SR top tag	40	37.7 ± 2.6	7.9 ± 0.6	27.6 ± 2.4	0.59 ± 0.07	1.0 ± 0.4	0.6 ± 1.2	2.54 ± 0.16	1.73 ± 0.12
3ℓ SR OF	4	4.3 ± 0.9	0.68 ± 0.11	3.4 ± 0.8	0.071 ± 0.034	0.07 ± 0.05	–	2.07 ± 0.16	0.69 ± 0.13

with 100% BR to the Z boson and a third-generation quark, T (B) masses up to 1.60 TeV (1.42 TeV) are excluded at 95% CL, while for the singlet and doublet configurations, masses are excluded up to 1.27 TeV (1.20 TeV) and up to 1.27 TeV (1.32 TeV), respectively. The combination of the two channels with their fine categorization results in the observed sensitivity, however, the limits are evidently driven by the categories with high expected signal-to-background fractions, namely, "2l 2b SR OF" (100%) and "3l SR OF" (45%).

Intermediate BR configurations are obtained by reweighting the simulated signal events to any target BR composition using generator-level information and assuming a total BR of 100% for the $T \rightarrow Zt$, $T \rightarrow Wb$, and $T \rightarrow Ht$ decay modes or the $B \rightarrow Zb$, $B \rightarrow Wt$, and $B \rightarrow Hb$ decay modes. The reweighting procedure allows 95% CL upper limits on the production cross-section to be set across the BR plane for each considered VLQ mass. By comparison with the theoretical prediction, lower limits on the T and B masses as a function of the BR composition can be obtained, as shown in Figure 8. As can be seen, the analysis is sensitive to a large subset of the possible BR compositions but the limits are more stringent closer to the lower-left corner of the BR plane, and thus for a higher BR for VLQ decays to a Z boson.

Table 4: Observed (expected) mass limits in TeV for the T and B singlet, doublet, and models with 100% BR to Z for the two channels and their combination.
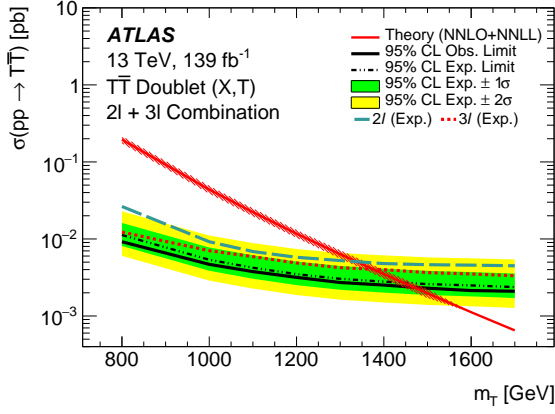
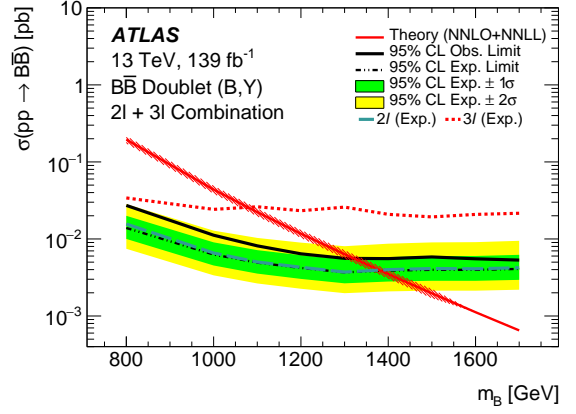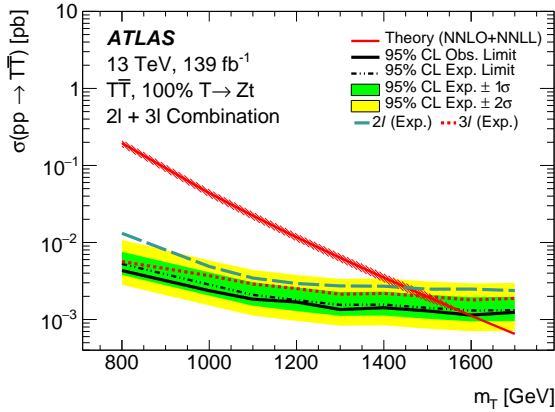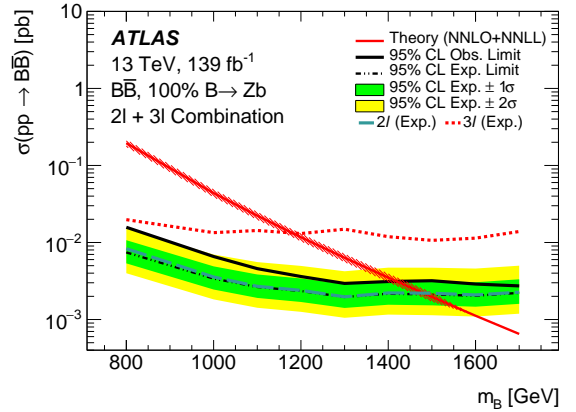| Model	Observed (Expected) Mass Limits [TeV]		
	2ℓ	3ℓ	Combination
$T\bar{T}$ Singlet	1.14 (1.16)	1.22 (1.21)	1.27 (1.28)
$T\bar{T}$ Doublet	1.34 (1.32)	1.38 (1.37)	1.46 (1.44)
100% $T \rightarrow Zt$	1.43 (1.43)	1.54 (1.50)	1.60 (1.56)
$B\bar{B}$ Singlet	1.14 (1.21)	1.11 (1.10)	1.20 (1.25)
$B\bar{B}$ Doublet	1.31 (1.37)	1.07 (1.04)	1.32 (1.38)
100% $B \rightarrow Zb$	1.40 (1.47)	1.16 (1.18)	1.42 (1.48)
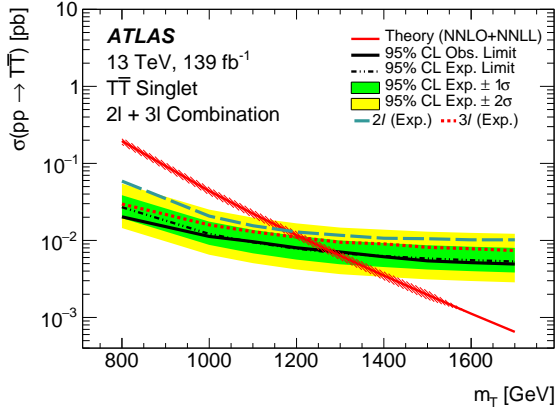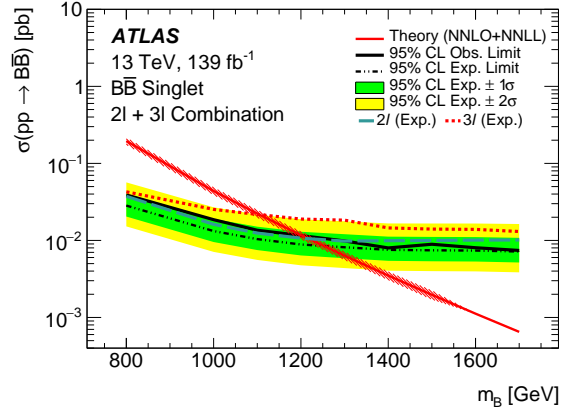
Figure 7: Expected and observed combined limits at 95% CL on the production cross-section for (a,c, and e) $T\bar{T}$ and (b,d, and f) $B\bar{B}$ for three representative BR compositions. The expected limits for the two individual channels are also shown.
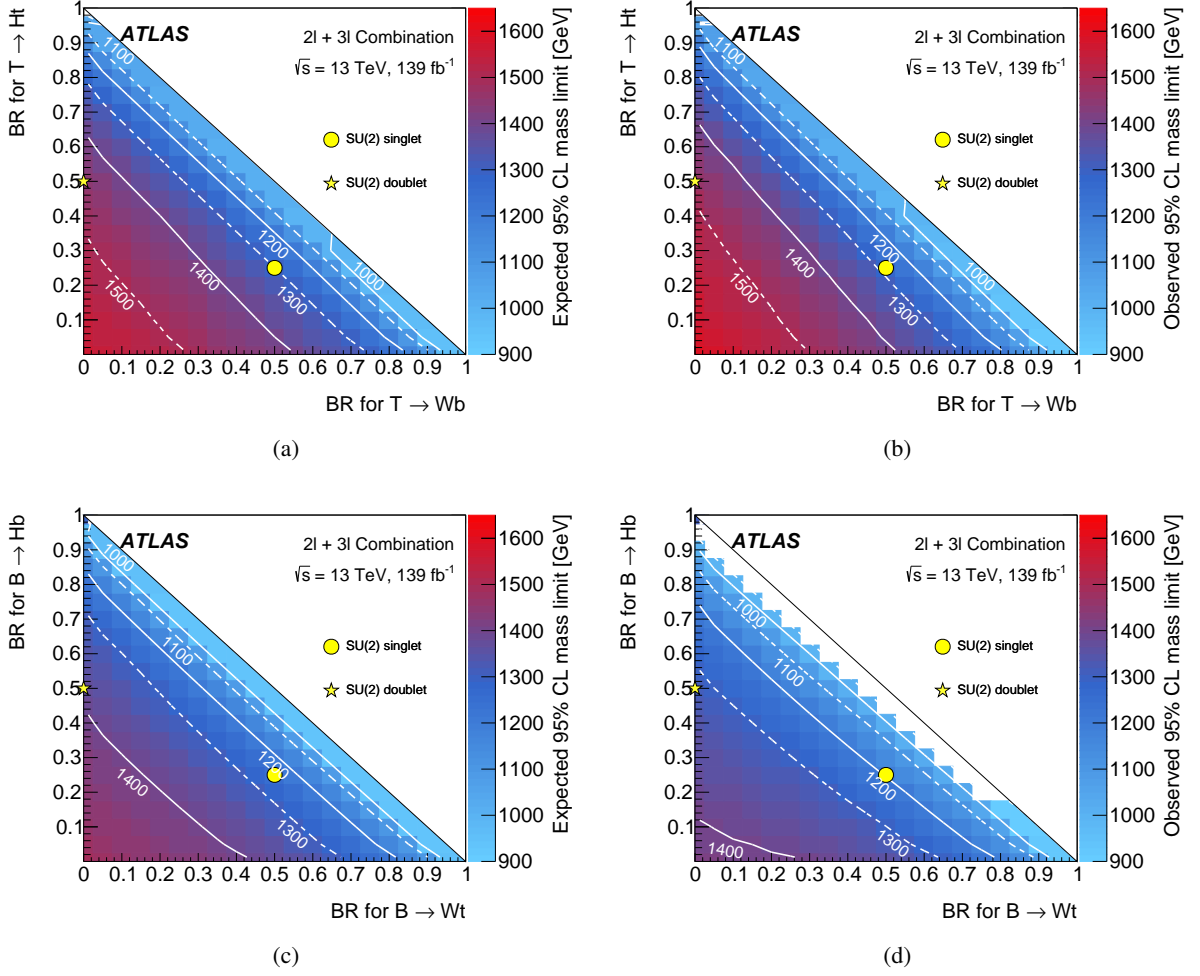
Figure 8: The (a,c) expected and (b,d) observed lower limits on the T and B masses at 95% CL in the BR plane from the combination of the two analysis channels for the production of (a,b) $T\bar{T}$ and (c,d) $B\bar{B}$, for all BR configurations when assuming a total BR of 100% for $T \to Zt$, $T \to Wb$, and $T \to Ht$ decays or $B \to Zb$, $B \to Wt$, and $B \to Hb$ decays, respectively. The white lines represent the contours of fixed m_{VLQ}.

8 Conclusions

A search for the pair production of vector-like quarks T or B, with electric charges $(2/3)e$ and $-(1/3)e$, respectively, is presented in which at least one of the VLQs decays into a leptonically decaying Z boson and a third-generation quark. Two orthogonal channels based on the number of selected leptons are separately optimized and their results are statistically combined to obtain the final result. In both channels a multi-class boosted object tagger for large-radius jets reclustered from smaller-radius jets is used to categorize events according to the numbers of V-tags, H-tags, and top-tags. The expected SM background is modelled with MC simulation and a maximum-likelihood fit to the data is performed. No significant excess over the background expectation is observed, and therefore 95% CL upper limits on the T and B pair-production cross-sections are derived.

The combined results exclude T (B) masses up to 1.27 TeV and 1.46 TeV (up to 1.20 TeV and 1.32 TeV) for the singlet and doublet configurations, respectively. For the doublet configuration, the lower limits on the T mass are extended by 90 GeV while the limits on the excluded T and B masses are extended by more than 200 GeV compared to the earlier ATLAS analysis using a subset of the Run 2 data.

References

[1] ATLAS Collaboration, *Observation of a new particle in the search for the Standard Model Higgs boson with the ATLAS detector at the LHC*, Phys. Lett. B **716** (2012) 1, arXiv: 1207.7214 [hep-ex].

[2] CMS Collaboration, *Observation of a new boson at a mass of 125 GeV with the CMS experiment at the LHC*, Phys. Lett. B **716** (2012) 30, arXiv: 1207.7235 [hep-ex].

[3] L. Susskind, *Dynamics of spontaneous symmetry breaking in the Weinberg-Salam theory*, Phys. Rev. D **20** (1979) 2619.

[4] D. B. Kaplan, H. Georgi and S. Dimopoulos, *Composite Higgs scalars*, Phys. Lett. B **136** (1984) 187.

[5] K. Agashe, R. Contino and A. Pomarol, *The minimal composite Higgs model*, Nucl. Phys. B **719** (2005) 165, arXiv: hep-ph/0412089 [hep-ph].

[6] N. Arkani-Hamed, A. G. Cohen, E. Katz and A. E. Nelson, *The Littlest Higgs*, JHEP **07** (2002) 034, arXiv: hep-ph/0206021 [hep-ph].

[7] M. Schmaltz and D. Tucker-Smith, *Little Higgs Theories*, Ann. Rev. Nucl. Part. Sci. **55** (2005) 229, arXiv: hep-ph/0502182 [hep-ph].

[8] F. del Aguila and M. J. Bowick, *The possibility of new fermions with $\Delta I = 0$ mass*, Nucl. Phys. B **224** (1983) 107.

[9] F. del Aguila, M. Perez-Victoria and J. Santiago, *Effective description of quark mixing*, Phys. Lett. B **492** (2000) 98, arXiv: hep-ph/0007160 [hep-ph].

[10] F. del Aguila, J. Santiago and M. Perez-Victoria, *Observable contributions of new exotic quarks to quark mixing*, JHEP **09** (2000) 011, arXiv: hep-ph/0007316 [hep-ph].

[11] J. A. Aguilar-Saavedra, *Identifying top partners at LHC*, JHEP **11** (2009) 030, arXiv: 0907.3155 [hep-ph].

[12] ATLAS Collaboration, *Combination of the searches for pair-produced vector-like partners of the third-generation quarks at $\sqrt{s} = 13$ TeV with the ATLAS detector*, Phys. Rev. Lett. **121** (2018) 211801, arXiv: 1808.02343 [hep-ex].

[13] ATLAS Collaboration, *Search for pair- and single-production of vector-like quarks in final states with at least one Z boson decaying into a pair of electrons or muons in pp collision data collected with the ATLAS detector*, Phys. Rev. D **98** (2018) 112010, arXiv: 1806.10555 [hep-ex].

[14] ATLAS Collaboration, *Search for pair production of heavy vector-like quarks decaying into hadronic final states in pp collisions at $\sqrt{s} = 13$ TeV with the ATLAS detector*, Phys. Rev. D **98** (2018) 092005, arXiv: 1808.01771 [hep-ex].

[15] ATLAS Collaboration, *Search for new phenomena in events with same-charge leptons and b-jets in pp collisions at $\sqrt{s} = 13$ TeV with the ATLAS detector*, JHEP **12** (2018) 039, arXiv: 1807.11883 [hep-ex].

[16] ATLAS Collaboration, *Search for pair production of heavy vector-like quarks decaying into high-p_T W bosons and top quarks in the lepton-plus-jets final state in pp collisions at $\sqrt{s} = 13$ TeV with the ATLAS detector*, JHEP **08** (2018) 048, arXiv: 1806.01762 [hep-ex].

[17] ATLAS Collaboration, *Search for pair production of up-type vector-like quarks and for four-top-quark events in final states with multiple b-jets with the ATLAS detector*, JHEP **07** (2018) 089, arXiv: 1803.09678 [hep-ex].

[18] ATLAS Collaboration, *Search for pair production of heavy vector-like quarks decaying to high-p_T W bosons and b quarks in the lepton-plus-jets final state in pp collisions at $\sqrt{s} = 13$ TeV with the ATLAS detector*, JHEP **10** (2017) 141, arXiv: 1707.03347 [hep-ex].

[19] ATLAS Collaboration, *Search for pair production of vector-like top quarks in events with one lepton, jets, and missing transverse momentum in $\sqrt{s} = 13$ TeV pp collisions with the ATLAS detector*, JHEP **08** (2017) 052, arXiv: 1705.10751 [hep-ex].

[20] CMS Collaboration, *Search for pair production of vector-like quarks in the fully hadronic final state*, Phys. Rev. D **100** (2019) 072001, arXiv: 1906.11903 [hep-ex].

[21] CMS Collaboration, *Search for vector-like quarks in events with two oppositely charged leptons and jets in proton–proton collisions at $\sqrt{s} = 13$ TeV*, Eur. Phys. J. C **79** (2019) 364, arXiv: 1812.09768 [hep-ex].

[22] CMS Collaboration, *Search for vector-like T and B quark pairs in final states with leptons at $\sqrt{s} = 13$ TeV*, JHEP **08** (2018) 177, arXiv: 1805.04758 [hep-ex].

[23] CMS Collaboration, *Search for pair production of vector-like quarks in the $bW\bar{b}W$ channel from proton–proton collisions at $\sqrt{s} = 13$ TeV*, Phys. Lett. B **779** (2018) 82, arXiv: 1710.01539 [hep-ex].

[24] CMS Collaboration, *A search for bottom-type, vector-like quark pair production in a fully hadronic final state in proton–proton collisions at $\sqrt{s} = 13$ TeV*, Phys. Rev. D **102** (2020) 112004, arXiv: 2008.09835 [hep-ex].

[25] A. Buckley, J. M. Butterworth, L. Corpe, D. Huang and P. Sun, *New sensitivity of current LHC measurements to vector-like quarks*, SciPost Phys. **9** (2020) 069, arXiv: 2006.07172 [hep-ph].

[26] ATLAS Collaboration, *Search for large missing transverse momentum in association with one top-quark in proton–proton collisions at $\sqrt{s} = 13$ TeV with the ATLAS detector*, JHEP **05** (2019) 041, arXiv: 1812.09743 [hep-ex].

[27] ATLAS Collaboration, *Search for single production of vector-like quarks decaying into Wb in pp collisions at $\sqrt{s} = 13$ TeV with the ATLAS detector*, JHEP **05** (2019) 164, arXiv: 1812.07343 [hep-ex].

[28] CMS Collaboration, *Search for electroweak production of a vector-like T quark using fully hadronic final states*, JHEP **01** (2020) 036, arXiv: 1909.04721 [hep-ex].

[29] CMS Collaboration, *Search for single production of vector-like quarks decaying to a top quark and a W boson in proton–proton collisions at $\sqrt{s} = 13$ TeV*, Eur. Phys. J. C **79** (2019) 90, arXiv: 1809.08597 [hep-ex].

[30] CMS Collaboration, *Search for single production of vector-like quarks decaying to a b quark and a Higgs boson*, JHEP **06** (2018) 031, arXiv: 1802.01486 [hep-ex].

[31] A. Roy, N. Nikiforou, N. Castro and T. Andeen, *Novel interpretation strategy for searches of singly produced vectorlike quarks at the LHC*, Phys. Rev. D **101** (2020) 115027, arXiv: 2003.00640 [hep-ph].

[32] ATLAS Collaboration, *The ATLAS Experiment at the CERN Large Hadron Collider*, JINST **3** (2008) S08003.

[33] ATLAS Collaboration, *ATLAS Insertable B-Layer Technical Design Report*, ATLAS-TDR-19; CERN-LHCC-2010-013, 2010, URL: https://cds.cern.ch/record/1291633, Addendum: ATLAS-TDR-19-ADD-1; CERN-LHCC-2012-009, 2012, URL: https://cds.cern.ch/record/1451888.

[34] B. Abbott et al., *Production and integration of the ATLAS Insertable B-Layer*, JINST **13** (2018) T05008, arXiv: 1803.00844 [physics.ins-det].

[35] ATLAS Collaboration, *Performance of the ATLAS trigger system in 2015*, Eur. Phys. J. C **77** (2017) 317, arXiv: 1611.09661 [hep-ex].

[36] ATLAS Collaboration, *The ATLAS Collaboration Software and Firmware*, ATL-SOFT-PUB-2021-001, 2021, URL: https://cds.cern.ch/record/2767187.

[37] ATLAS Collaboration, *The ATLAS Simulation Infrastructure*, Eur. Phys. J. C **70** (2010) 823, arXiv: 1005.4568 [physics.ins-det].

[38] GEANT4 Collaboration, S. Agostinelli et al., *GEANT4 – a simulation toolkit*, Nucl. Instrum. Meth. A **506** (2003) 250.

[39] T. Gleisberg et al., *Event generation with SHERPA 1.1*, JHEP **02** (2009) 007, arXiv: 0811.4622 [hep-ph].

[40] S. Höche, F. Krauss, S. Schumann and F. Siegert, *QCD matrix elements and truncated showers*, JHEP **05** (2009) 053, arXiv: 0903.1219 [hep-ph].

[41] T. Gleisberg and S. Höche, *Comix, a new matrix element generator*, JHEP **12** (2008) 039, arXiv: 0808.3674 [hep-ph].

[42] S. Schumann and F. Krauss, *A parton shower algorithm based on Catani–Seymour dipole factorisation*, JHEP **03** (2008) 038, arXiv: 0709.1027 [hep-ph].

[43] R. D. Ball et al., *Parton distributions for the LHC run II*, JHEP **04** (2015) 040, arXiv: 1410.8849 [hep-ph].

[44] C. Anastasiou, L. Dixon, K. Melnikov and F. Petriello, *High-precision QCD at hadron colliders: Electroweak gauge boson rapidity distributions at next-to-next-to leading order*, Phys. Rev. D **69** (2004) 094008, arXiv: hep-ph/0312266.

[45] F. Cascioli, P. Maierhöfer and S. Pozzorini, *Scattering Amplitudes with Open Loops*, Phys. Rev. Lett. **108** (2012) 111601, arXiv: 1111.5206 [hep-ph].

[46] S. Höche, F. Krauss, M. Schönherr and F. Siegert, *QCD matrix elements + parton showers. The NLO case*, JHEP **04** (2013) 027, arXiv: 1207.5030 [hep-ph].

[47] J. Alwall et al., *The automated computation of tree-level and next-to-leading order differential cross sections, and their matching to parton shower simulations*, JHEP **07** (2014) 079, arXiv: 1405.0301 [hep-ph].

[48] T. Sjöstrand et al., *An introduction to PYTHIA 8.2*, Comput. Phys. Commun. **191** (2015) 159, arXiv: 1410.3012 [hep-ph].

[49] ATLAS Collaboration, *ATLAS Pythia 8 tunes to 7 TeV data*, ATL-PHYS-PUB-2014-021, 2014, URL: https://cds.cern.ch/record/1966419.

[50] P. Nason, *A new method for combining NLO QCD with shower Monte Carlo algorithms*, JHEP **11** (2004) 040, arXiv: hep-ph/0409146.

[51] S. Frixione, P. Nason and C. Oleari, *Matching NLO QCD computations with parton shower simulations: the POWHEG method*, JHEP **11** (2007) 070, arXiv: 0709.2092 [hep-ph].

[52] S. Alioli, P. Nason, C. Oleari and E. Re, *A general framework for implementing NLO calculations in shower Monte Carlo programs: the POWHEG BOX*, JHEP **06** (2010) 043, arXiv: 1002.2581 [hep-ph].

[53] J. M. Campbell, R. K. Ellis, P. Nason and E. Re, *Top-Pair Production and Decay at NLO Matched with Parton Showers*, JHEP **04** (2015) 114, arXiv: 1412.1828 [hep-ph].

[54] M. Czakon and A. Mitov, *Top++: A program for the calculation of the top-pair cross-section at hadron colliders*, Comput. Phys. Commun. **185** (2014) 2930, arXiv: 1112.5675 [hep-ph].

[55] M. Czakon, P. Fiedler and A. Mitov, *Total Top-Quark Pair-Production Cross Section at Hadron Colliders Through $O(\alpha_S^4)$*, Phys. Rev. Lett. **110** (2013) 252004, arXiv: 1303.6254 [hep-ph].

[56] M. Beneke, P. Falgari, S. Klein and C. Schwinn, *Hadronic top-quark pair production with NNLL threshold resummation*, Nucl. Phys. B **855** (2012) 695, arXiv: 1109.1536 [hep-ph].

[57] M. Cacciari, M. Czakon, M. Mangano, A. Mitov and P. Nason, *Top-pair production at hadron colliders with next-to-next-to-leading logarithmic soft-gluon resummation*, Phys. Lett. B **710** (2012) 612, arXiv: 1111.5869 [hep-ph].

[58] M. Czakon and A. Mitov, *NNLO corrections to top pair production at hadron colliders: the quark-gluon reaction*, JHEP **01** (2013) 080, arXiv: 1210.6832 [hep-ph].

[59] M. Czakon and A. Mitov, *NNLO corrections to top-pair production at hadron colliders: the all-fermionic scattering channels*, JHEP **12** (2012) 054, arXiv: 1207.0236 [hep-ph].

[60] P. Bärnreuther, M. Czakon and A. Mitov, *Percent-Level-Precision Physics at the Tevatron: Next-to-Next-to-Leading Order QCD Corrections to $q\bar{q} \to t\bar{t} + X$*, Phys. Rev. Lett. **109** (2012) 132001, arXiv: 1204.5201 [hep-ph].

[61] J. Bellm et al., *Herwig 7.0/Herwig++ 3.0 release note*, Eur. Phys. J. C **76** (2016) 196, arXiv: 1512.01178 [hep-ph].

[62] R. Frederix, D. Pagani and M. Zaro, *Large NLO corrections in $t\bar{t}W^{\pm}$ and $t\bar{t}t\bar{t}$ hadroproduction from supposedly subleading EW contributions*, JHEP **02** (2018) 031, arXiv: 1711.02116 [hep-ph].

[63] R. Frederix, E. Re and P. Torrielli, *Single-top t-channel hadroproduction in the four-flavour scheme with POWHEG and aMC@NLO*, JHEP **09** (2012) 130, arXiv: 1207.5391 [hep-ph].

[64] E. Re, *Single-top Wt-channel production matched with parton showers using the POWHEG method*, Eur. Phys. J. C **71** (2011) 1547, arXiv: 1009.2450 [hep-ph].

[65] M. Aliev et al., *HATHOR – HAdronic Top and Heavy quarks crOss section calculatoR*, Comput. Phys. Commun. **182** (2011) 1034, arXiv: 1007.1327 [hep-ph].

[66] P. Kant et al., *HatHor for single top-quark production: Updated predictions and uncertainty estimates for single top-quark production in hadronic collisions*, Comput. Phys. Commun. **191** (2015) 74, arXiv: 1406.4403 [hep-ph].

[67] N. Kidonakis, *Next-to-next-to-leading-order collinear and soft gluon corrections for t-channel single top quark production*, Phys. Rev. D **83** (2011) 091503, arXiv: 1103.2792 [hep-ph].

[68] N. Kidonakis, *Two-loop soft anomalous dimensions for single top quark associated production with a W^- or H^-*, Phys. Rev. D **82** (2010) 054018, arXiv: 1005.4451 [hep-ph].

[69] N. Kidonakis, *Next-to-next-to-leading logarithm resummation for s-channel single top quark production*, Phys. Rev. D **81** (2010) 054028, arXiv: 1001.5034 [hep-ph].

[70] S. Frixione, E. Laenen, P. Motylinski, C. White and B. R. Webber, *Single-top hadroproduction in association with a W boson*, JHEP **07** (2008) 029, arXiv: 0805.3067 [hep-ph].

[71] J. A. Aguilar-Saavedra, *Protos - PROgram for TOp Simulations*, URL: http://jaguilar.web.cern.ch/jaguilar/protos.

[72] A. D. Martin, W. J. Stirling, R. S. Thorne and G. Watt, *Parton distributions for the LHC*, Eur. Phys. J. C **63** (2009) 189, arXiv: `0901.0002 [hep-ph]`.

[73] A. D. Martin, W. J. Stirling, R. S. Thorne and G. Watt, *Uncertainties on α_S in global PDF analyses and implications for predicted hadronic cross sections*, Eur. Phys. J. C **64** (2009) 653, arXiv: `0905.3531 [hep-ph]`.

[74] A. D. Martin, W. J. Stirling, R. S. Thorne and G. Watt, *Heavy-quark mass dependence in global PDF analyses and 3- and 4-flavour parton distributions*, Eur. Phys. J. C **70** (2010) 51, arXiv: `1007.2624 [hep-ph]`.

[75] ATLAS Collaboration, *Electron and photon performance measurements with the ATLAS detector using the 2015–2017 LHC proton–proton collision data*, JINST **14** (2019) P12006, arXiv: `1908.00005 [hep-ex]`.

[76] ATLAS Collaboration, *Muon reconstruction and identification efficiency in ATLAS using the full Run 2 pp collision data set at $\sqrt{s}$ = 13 TeV*, Eur. Phys. J. C **81** (2021) 578, arXiv: `2012.00578 [hep-ex]`.

[77] M. Cacciari, G. P. Salam and G. Soyez, *The anti-k_t jet clustering algorithm*, JHEP **04** (2008) 063, arXiv: `0802.1189 [hep-ph]`.

[78] M. Cacciari, G. P. Salam and G. Soyez, *FastJet user manual*, Eur. Phys. J. C **72** (2012) 1896, arXiv: `1111.6097 [hep-ph]`.

[79] ATLAS Collaboration, *Topological cell clustering in the ATLAS calorimeters and its performance in LHC Run 1*, Eur. Phys. J. C **77** (2017) 490, arXiv: `1603.02934 [hep-ex]`.

[80] ATLAS Collaboration, *Properties of jets and inputs to jet reconstruction and calibration with the ATLAS detector using proton–proton collisions at $\sqrt{s}$ = 13 TeV*, ATL-PHYS-PUB-2015-036, 2015, URL: `https://cds.cern.ch/record/2044564`.

[81] ATLAS Collaboration, *Jet energy scale measurements and their systematic uncertainties in proton–proton collisions at $\sqrt{s}$ = 13 TeV with the ATLAS detector*, Phys. Rev. D **96** (2017) 072002, arXiv: `1703.09665 [hep-ex]`.

[82] ATLAS Collaboration, *Performance of pile-up mitigation techniques for jets in pp collisions at $\sqrt{s}$ = 8 TeV using the ATLAS detector*, Eur. Phys. J. C **76** (2016) 581, arXiv: `1510.03823 [hep-ex]`.

[83] ATLAS Collaboration, *ATLAS b-jet identification performance and efficiency measurement with $t\bar{t}$ events in pp collisions at $\sqrt{s}$ = 13 TeV*, Eur. Phys. J. C **79** (2019) 970, arXiv: `1907.05120 [hep-ex]`.

[84] ATLAS Collaboration, *Performance of missing transverse momentum reconstruction with the ATLAS detector using proton–proton collisions at $\sqrt{s}$ = 13 TeV*, Eur. Phys. J. C **78** (2018) 903, arXiv: `1802.08168 [hep-ex]`.

[85] B. Nachman, P. Nef, A. Schwartzman, M. Swiatlowski and C. Wanotayaroj, *Jets from Jets: Re-clustering as a tool for large radius jet reconstruction and grooming at the LHC*, JHEP **02** (2015) 075, arXiv: `1407.2922 [hep-ph]`.

[86] D. Krohn, J. Thaler and L.-T. Wang, *Jet trimming*, JHEP **02** (2010) 084, arXiv: `0912.1342 [hep-ph]`.

[87] ATLAS Collaboration, *Performance of the ATLAS muon triggers in Run 2*, JINST **15** (2020) P09015, arXiv: `2004.13447 [hep-ex]`.

[88]   ATLAS Collaboration, *Performance of electron and photon triggers in ATLAS during LHC Run 2*, Eur. Phys. J. C **80** (2020) 47, arXiv: 1909.00761 [hep-ex].

[89]   F. Chollet et al., *Keras*, 2015, URL: https://keras.io.

[90]   Martín Abadi et al., *TensorFlow: Large-Scale Machine Learning on Heterogeneous Systems*, 2015, URL: https://www.tensorflow.org/.

[91]   K. Agashe, H. Davoudiasl, G. Perez and A. Soni, *Warped gravitons at the CERN LHC and beyond*, Phys. Rev. D **76** (2007) 036006, arXiv: hep-ph/0701186.

[92]   J. Schmidhuber, *Deep learning in neural networks: An overview*, Neural Networks **61** (2015) 85.

[93]   I. Goodfellow, Y. Bengio and A. Courville, *Deep Learning*, http://www.deeplearningbook.org, MIT Press, 2016.

[94]   D. P. Kingma and J. Ba, *Adam: A Method for Stochastic Optimization*, 2014, arXiv: 1412.6980 [cs.LG].

[95]   ATLAS Collaboration, *Optimisation of large-radius jet reconstruction for the ATLAS detector in 13 TeV proton–proton collisions*, Eur. Phys. J. C **81** (2020) 334, arXiv: 2009.04986 [hep-ex].

[96]   ATLAS Collaboration, *Measurement of the c-jet mistagging efficiency in $t\bar{t}$ events using pp collision data at $\sqrt{s}$ = 13 TeV collected with the ATLAS detector*, Eur. Phys. J. C **82** (2021) 95, arXiv: 2109.10627 [hep-ex].

[97]   ATLAS Collaboration, *Calibration of light-flavour b-jet mistagging rates using ATLAS proton–proton collision data at $\sqrt{s}$ = 13 TeV*, ATLAS-CONF-2018-006, 2018, URL: https://cds.cern.ch/record/2314418.

[98]   ATLAS Collaboration, *Luminosity determination in pp collisions at $\sqrt{s}$ = 13 TeV using the ATLAS detector at the LHC*, ATLAS-CONF-2019-021, 2019, URL: https://cds.cern.ch/record/2677054.

[99]   ATLAS Collaboration, *Measurements of the inclusive and differential production cross sections of a top-quark-antiquark pair in association with a Z boson at $\sqrt{s}$ = 13 TeV with the ATLAS detector*, Eur. Phys. J. C **81** (2021) 737, arXiv: 2103.12603 [hep-ex].

[100] ATLAS Collaboration, *Higgs boson production cross-section measurements and their EFT interpretation in the 4ℓ decay channel at $\sqrt{s}$ = 13 TeV with the ATLAS detector*, Eur. Phys. J. C **80** (2020) 957, arXiv: 2004.03447 [hep-ex], Erratum: Eur. Phys. J. C **81** (2021) 29.

[101] J. Butterworth et al., *PDF4LHC recommendations for LHC Run II*, J. Phys. G **43** (2016) 023001, arXiv: 1510.03865 [hep-ph].

[102] H.-L. Lai et al., *New parton distributions for collider physics*, Phys. Rev. D **82** (2010) 074024, arXiv: 1007.2241 [hep-ph].

[103] J. Gao et al., *CT10 next-to-next-to-leading order global analysis of QCD*, Phys. Rev. D **89** (2014) 033009, arXiv: 1302.6246 [hep-ph].

[104] G. Cowan, K. Cranmer, E. Gross and O. Vitells, *Asymptotic formulae for likelihood-based tests of new physics*, Eur. Phys. J. C **71** (2011) 1554, arXiv: 1007.1727 [physics.data-an], Erratum: Eur. Phys. J. C **73** (2013) 2501.

[105] L. Moneta et al., *The RooStats Project*, PoS **ACAT2010** (2010) 057, ed. by T. Speer et al., arXiv: 1009.1003 [physics.data-an].

[106] W. Verkerke and D. Kirkby, *The RooFit toolkit for data modeling*, 2003, arXiv: `physics/0306116 [physics.data-an]`.

[107] K. Cranmer, G. Lewis, L. Moneta, A. Shibata and W. Verkerke, *HistFactory: A tool for creating statistical models for use with RooFit and RooStats*, tech. rep., New York U., 2012, URL: `https://cds.cern.ch/record/1456844`.

[108] T. Junk, *Confidence level computation for combining searches with small statistics*, Nucl. Instrum. Meth. A **434** (1999) 435, arXiv: `hep-ex/9902006 [hep-ex]`.

[109] A. L. Read, *Presentation of search results: the CL_S technique*, J. Phys. G **28** (2002) 2693.